

In-situ Printability Maps (IPM): A new approach for in-situ printability assessment with application to extrusion-based bioprinting

Giovanni Zanderigo¹, Filippo Bracco¹, Quirico Semeraro, Bianca Maria Colosimo^{*}

Department of Mechanical Engineering, Politecnico di Milano, Via La Masa, 1, 20156, Milano, Italy

ARTICLE INFO

Keywords:

Additive manufacturing
3D bioprinting
In-situ process optimization
Extrusion bioprinting
Printability assessment

ABSTRACT

3D Bioprinting is an emerging field with many highly valuable applications. The most common and versatile technology is extrusion-based bioprinting, which requires extensive experimental campaigns to achieve appropriate quality of the bioprinted constructs when new bioinks or complex geometrical constructs need to be considered. This paper presents a new approach to easily guide operators and scientists to evaluate the probability of successful bioprinting in a defined window of the process parameters, starting from a small experimental campaign and relying on in-situ quality data. The proposed method consists of defining printability maps based on a probabilistic approach. These maps assess the printing outcome considering a specified acceptable deviation from the nominal geometry, which is predefined by the end-user depending on the application at hand. Even if shown with reference to extrusion-based bioprinting, the proposed method can be used with any other bioprinting process and any quality index, including categorical assessment classification. Eventually, the paper shows how the map can be combined with different quality criteria (e.g., productivity, cell viability) to define the appropriate setting, depending on the application at hand. Furthermore, the map provides a practical tool for rapid material printability assessment and robust process optimization. It offers an enhanced visual representation of the process domain, acceptable region boundaries, and their resilience to variation and uncertainties. Eventually, in-situ printability maps represent a further leap for the advancement of bioprinting toward the digital transformation, aiming at increasing the controllability and scalability of the bioprinting process.

1. Introduction

The applications of 3D Bioprinting (3DBP) are vast, spanning from life sciences to tissue engineering, drug delivery, and food bioprinting [1,2]. Various techniques are employed in 3DBP, such as nozzle-deposition (extrusion and inkjet) and optical-based methods (vat photopolymerisation and two-photon polymerisation). Among these, extrusion-based bioprinting is the most common and extensively studied [1]. This technique involves material extrusion through pneumatic pressure or screw-driven force, enabling the use of a wide range of materials at affordable costs.

Due to its flexibility, extrusion-based bioprinting accommodates numerous bioinks and cell lines. Consequently, assessing printability has become essential to ensure geometric accuracy and to study the relationships between material properties and process parameters.

Printability, a critical aspect in bioprinting, encompasses extrudability, filament fidelity, and structural fidelity, as outlined by Fu et al.

[3]. These parameters are influenced by the process (crosslinking strategy, process parameters), bioink (rheological and physical properties, formulation), and construct design [3]. Table 1 provides an overview of various approaches to printability assessment, categorized by type.

Early studies in bioprinting primarily focused on the rheological and mechanical properties of bioinks [4–7]. Parameters such as storage (G') and loss (G'') moduli, viscosity, and yield shear stress were explored to predict shape fidelity and cell viability [8,9]. High storage modulus values positively correlated with shape fidelity but negatively impacted extrudability and cell viability. Conversely, the loss modulus inversely affected material spreading after printing. Viscosity, crucial for extrudability and cell viability, led to the preference for shear thinning materials to prevent nozzle clogging during extrusion. Additionally, a high yield shear stress positively influenced the self-standing property of multilayer constructs but adversely affected material extrudability. Freeman et al. [10] proposed a recommended range of rheological properties for bioinks used in extrusion-based bioprinting.

^{*} Corresponding author. Via La Masa 1, 20156, Milano, Italy.

E-mail address: biancamaria.colosimo@polimi.it (B.M. Colosimo).

¹ . These authors contributed equally to this work.

Abbreviations			
3DBP	3D Bioprinting	IPM	In-situ Printability Maps
ACF	Autocorrelation Function	LBQ	Ljung-Box Q-Test
ALGEL	Alginate + Gelatine ink	LSL	Lower Specification Limit
AM	Additive Manufacturing	ML	Machine Learning
DMEM	Dulbecco's Modified Eagle Medium	MSE	Mean Square Error
DOE	Design of Experiment	OLS	Ordinary Least Square regression
FBS	Fetal Bovine Serum	P	Pressure, [kPa]
FD	Filament Diameter	PBS	Phosphate-Buffered Saline
FF	Filament Fusion	PI	Pore Index
F_{T,df}	Student's T cumulative distribution function	ROI	Region of Interest
GLM	Generalized Linear Model	USL	Upper Specification Limit
		V	Speed, [mm/s]

However, rheological parameters are just the starting point, laying the foundation for the preliminary design [11]. Process-related factors profoundly influence the final print quality. This paper focuses on guiding process optimization through in-situ data, aiming to identify the optimal process parameters for shape fidelity in bioprinting. Building upon seminal works by Ouyang [12] and Paxton [13], researchers have introduced printability indexes to assess bioprinted job quality, considering aspects like temperature and cell viability [14–20]. Some studies have incorporated physical models of materials to enhance prediction accuracy [21–23]. Yet, physical models necessitate in-depth material parameter knowledge, obtained through dedicated experimental campaigns. Empirical models, based on experimental data, have also been introduced to link printing outcomes with process parameters, opening avenues for in-situ process optimization [24–29].

In recent years, Machine Learning (ML) has emerged as a powerful tool for identifying optimal printing conditions. ML algorithms have been implemented at various stages of the printing process. Shin et al. [30] pioneered the use of ML to optimize biomaterial design for achieving optimal printing conditions ex-ante, meaning before printing begins. Ruberu et al. [31] proposed a Bayesian optimization approach to determine the best printing conditions by observing process outcomes after printing, employing ex-situ assessments. Bonatti et al. [32] introduced an innovative ML solution for quality control in extrusion-based bioprinting, utilizing video images captured by a webcam placed in front of printers at different distances. In this approach, a Convolutional Neural Network (CNN) model was trained using a substantial dataset of video images, with a tuning feature based on the deposited material volume employed for process optimization. In contrast to this previous work, our approach takes a distinct perspective. Firstly, we concentrate on the final quality of the bioprinted object, considering not only the extruded material observed from the nozzle but also the deposition speed and material-layer interactions. Our objective is to enhance the overall quality of the bioprinted job, accounting for factors such as pressure/speed of material extrusion, deposition speed, and material-layer interactions. Secondly, our method does not rely on an extensive dataset for training. Instead, it is based on a focused experimental campaign designed to explore the parameter space. While ML and CNNs are valuable when dealing with highly nonlinear relationships between response functions and process parameters, this complexity does not seem prevalent in the context of bioprinting explored in our framework. Furthermore, employing ML typically demands substantial data (training sets) and results in non-interpretable, black-box models [33]. These models are usually necessary for investigating intricate relationships. However, in our case, a simpler and more interpretable model suffices. By focusing on a targeted experimental approach, we aim to provide insights into the bioprinting process while maintaining the interpretability of the results. In summary, while ML remains a promising avenue for optimizing bioprinting processes, our approach seeks to strike a balance. By concentrating on essential parameters and

employing focused experimental campaigns, we aim to enhance the quality and interpretability of bioprinted outcomes, thereby contributing to the ongoing evolution of 3D bioprinting technologies.

This paper introduces a pioneering methodology for creating a robust printability map and demonstrates its application in extrusion-based bioprinting. The term “robustness” in this context refers to a predefined level of deviation from the nominal shape that is acceptable in the construction of the printability map. Bioprinting, unlike other sectors such as aerospace or biomedical implants, allows for controlled deviations from the nominal geometry, making geometrical accuracy less stringent. To accommodate this, the user can define a tolerance interval with Upper and Lower Specification Limits (USL and LSL, respectively) within which the quality indicator of interest can vary without affecting the overall performance of the bioprinted construct. This approach draws inspiration from iso-probability maps used in metal additive manufacturing for lattice structures [34].

Starting from this seminal concept, our methodology defines the In-situ Printability Map (IPM) to correlate bioprinting process parameters with the final quality of printed constructs. The printability map, grounded in empirical data, incorporates prediction uncertainty arising from natural randomness in experimental data. It calculates the probability of creating a construct meeting specification limits for each parameter space location. Specifically, pressure and extrusion speed are considered as process parameters. Robust printability maps are presented for both quantitative indicators (e.g., pore index) and qualitative indicators (e.g., visual assessment of filament fusion) to identify optimal regions satisfying multiple objectives. A sensitivity analysis regarding the specification interval is conducted to understand how tolerated deviations from the nominal shape influence the size and location of the optimal printability region.

To showcase the practical use of these maps in bioprinting, a cell viability assessment is performed within regions ensuring shape fidelity. This proposed approach establishes a hierarchical bioprinting method: i) an initial printability map considering only the bioink without cells for preliminary exploration and minimizing cell damage; ii) a subsequent step where the most promising locations from robust printability maps are evaluated to select optimal conditions for cell viability. The outcome is a streamlined procedure utilizing IPMs as a potent tool to identify promising process domains and pinpoint optimal operating conditions in bioprinting. Although the study focuses on specific applications, the approach is versatile and adaptable to various bioprinting technologies.

The paper is organized as follows: Section 2 presents the comprehensive methodology, encompassing bioink preparation, construct design, printing setup, quality index definitions, and in-situ image acquisition. Section 3 delves into the proposed approach, detailing probabilistic printability maps for different natured quality indexes, quantitative and categorical. A final discussion and viability assessment are provided in Sections 4 and 5. The paper concludes with insights in the final section.

Table 1
Different approaches for printability assessment in extrusion-based bioprinting.

Paper	Rehological analysis	Qualitative printability assessment	Quantitative evaluation of printability indexes	Presence of material physical models	Empirical model fitting	Machine Learning
Naitre et al. [4]	✓					✓
Gao et al. [5]	✓					✓
Chung et al. [6]	✓					
Zhao et al. [7]	✓					
Gillispie et al. [14]	✓					
Ouyang et al. [12]	✓					
Paxton et al. [13]	✓					
Habib et al. [15]	✓					
Moncal et al. [16]	✓					
Sawyer et al. [17]	✓	✓	✓	✓		
He et al. [18]	✓	✓	✓	✓		
Nelson et al. [19]	✓	✓	✓	✓		
Hibbert et al. [20]	✓	✓	✓	✓		
Sun et al. [22]	✓					✓
Ribero et al. [21]	✓	✓	✓	✓	✓	
Temiret et al. [23]	✓	✓	✓	✓	✓	
Coskun et al. [24]	✓	✓	✓	✓		
Armstrong et al. [25]	✓	✓	✓	✓	✓	
Gao et al. [26]	✓					
Trachtenberg et al. [27]	✓					
Armstrong et al. [29]	✓					
Armstrong et al. [28]	✓					
Shin et al. [28]	✓					
Rubio et al. [29]	✓					
Bonafant et al. [30]	✓					

2. Materials and methods

2.1. Bioink and bioprinter

Given the significance of bioprinting in the realm of cultured meat production, the material chosen for the case study is one of the edible biomaterials commonly utilized in tissue engineering. The bioink comprises Alginate combined with Gelatin, aiming to incorporate an RGD-containing polypeptide into the polysaccharide structure [35].

To prepare the bioink, two stock solutions were created. An 8 % (w/v) Sodium Alginate stock solution was formed by dissolving Sodium Alginate (Sigma Aldrich) in sterile PBS, which was then continuously stirred at 50 °C for 4 h using a heated magnetic stirrer. Additionally, a 16 % (w/v) Gelatin stock solution was made by dissolving Gelatin (Sigma Aldrich) in sterile PBS and stirring the solution at 30 °C for 4 h with a heated magnetic stirrer. These solutions were refrigerated overnight for complete hydration.

The bioink, referred to as AlGel, was produced by diluting 6 % Alginate and 4 % Gelatin in a 3:1 ratio, resulting in a 40 ml solution. To half of this ink (20 ml), 2 ml of a 10 % (w/v) Amaranth solution was added to give the ink a vivid red color. The remaining 20 ml of AlGel solution was kept for subsequent viability assessments with cells. The addition of Amaranth served two purposes: it aided image segmentation during analysis and simulated the addition of a 10 % cell suspension solution to the bioink, following the Cellink protocol. This allowed us to conduct printability assessments without cells while mimicking the rheology of cell-laden bioink, as low cell densities do not significantly impact the final bioink rheology [36]. The mixture was stirred with a magnetic stirrer until a homogeneous color was achieved.

The bioprinting process utilized the BIO X™ printer (Cellink®) equipped with a pneumatic extruder with temperature control. The printer was loaded with 3 ml cartridges (Cellink®) featuring a conical nozzle with a diameter of 0.410 mm (Cellink®). In-situ images were captured using the HD Camera Tool (Cellink®) provided by the bioprinter manufacturer. To enhance image quality, an external ring light was used during image acquisition.

2.2. Cell culture and viability assessment

C2C12 murine myoblasts were cultured in DMEM (Sigma Aldrich), supplemented with 10 % fetal bovine serum (FBS, Sigma Aldrich), 1 % penicillin/streptomycin, and 1 % glutamine, maintaining the cultures at 37 °C with 5 % CO₂. Upon reaching 80 % confluency, the cells were detached and prepared for the experiment. Cell counting was conducted using LUNA™ Cell Counting Slides and the automated cell counting function of the CELENA® S microscope.

For viability assessment in the presence of cells, the bioprinter was positioned within a biological hood and sterilized with UV light for 1 h prior to the experiment. The bioink and cells were mixed according to the Cellink protocol, achieving a cell density of 2.5×10^5 cells/mL. Constructs were printed and crosslinked using a CaCl₂ solution (50 mM, Cellink®) bath for 5 min. Subsequently, the crosslinking solution was removed, and complete DMEM medium was added. Plates were then incubated at 37 °C with 5 % CO₂.

Cell viability was determined using fluorescence Live/Dead staining, incorporating calcein (2 µM), propidium iodide (0.5 µM), and DAPI (0.3 µM) in the medium. The culture medium was replaced with the Live/Dead staining solution and incubated for 40 min. Samples were analyzed using the CELENA® S Fluorescence Microscope. Images were digitally filtered, and viability was calculated as the ratio of live cells to the total cell count.

2.3. Design of Experiment

Several process parameters were taken into consideration for the experiment, including extrusion temperature and pressure, scanning speed of the print head, and design parameters such as nozzle size and layer height. Among these, temperature, pressure, and speed were

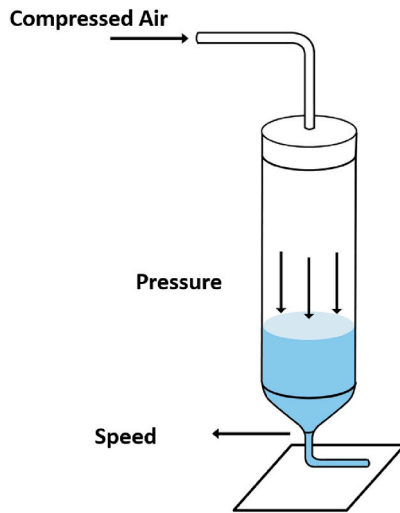


Fig. 1. Influence of the two factors on the extrusion process.

identified as the most influential through an initial experimental screening campaign. Temperature was then maintained at a constant level due to challenges in controlling it throughout the entire print chamber and was treated as a nuisance variable to ensure the creation of a robust and reliable model. Consequently, the experiment was structured based on a two-factors factorial Design of Experiment (DoE) [37]. The two primary process parameters analyzed were extrusion Pressure (P) and the scanning speed (V) of the printhead, as illustrated in Fig. 1.

For both the factors, 6 levels were explored, namely: $P \in [5, 10, 15, 20, 25, 30] \text{ kPa}$ and $V \in [5, 10, 15, 20, 25, 30] \text{ mm/s}$. The speed upper limit was chosen due to the stability limit of the machine, while the pressure upper limit was chosen to avoid overextrusion based on previous printing experiences. Each combination of parameters was randomly replicated 3 times, for a total of 108 experimental observations.

2.4. Printability assessment

To evaluate printability, three distinct quality indexes were initially measured. The first was the Pore Index (PI), indicating the shape fidelity of the printed construct. The second was Filament Fusion (FF), representing the tendency of adjacent filaments to merge [12]. Finally, Filament Diameter (FD) was also considered, although it was ultimately excluded from the analysis due to its high correlation with PI, rendering additional analysis redundant.

To calculate the printability parameters, the 3D model of the construct was meticulously designed to incorporate specific regions for evaluating each parameter independently (Fig. 2). The printed object was crafted to feature a filled area on the left, which would be translated into a net-like geometry (Fig. 2a) by the CAM software of the bioprinter. Additionally, at the center, a parallel filament geometry with decreasing hatch distance was incorporated (Fig. 2b). To facilitate image analysis, the geometry was designed as a monolayer, perfectly fitting the field of view of the HD camera ($20 \times 20 \text{ mm}$). Consequently, the final dimensions of the printed geometry were $15 \times 16 \times 0.5 \text{ mm}$.

In existing literature, various methods for assessing shape fidelity have been proposed. In our study, we evaluated the Pore Index (PI) on a net-like geometry using the following formula:

$$PI = \frac{A_i}{A} \quad 1$$

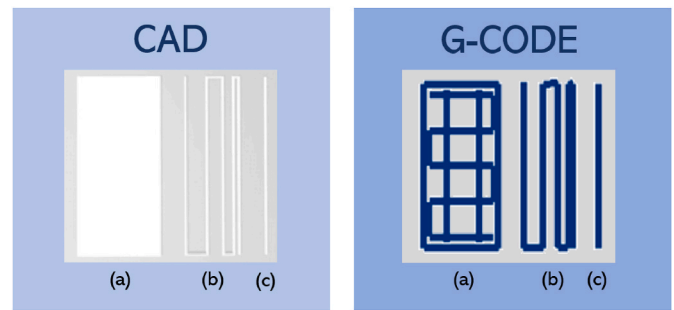


Fig. 2. The input model STL (left), and the output G-Code (right). The model has been designed to contain portions for the assessment of PI (a), FF (b), and a single filament (c).

where A_i represents the real area of the i -th printed grid void, and A is the ideal area of the printed grid void gathered from the G-code.

To assess PI, the image was divided into four small Regions of Interest (ROI) around the grid voids. Each ROI was analyzed using a region-growing algorithm [38] to estimate the grid void's area. PI values were calculated for each of the four areas, as displayed in the dedicated tab of Fig. 3. Subsequently, their mean value was utilized for further analysis.

Filament Fusion (FF) was evaluated on a series of parallel filaments designed with decreasing hatching distances: 2 mm, 1.5 mm, and 1 mm (between filament axes). FF was estimated by determining the smallest distance between adjacent filaments that prevented merging [12], ranging from 0 (meaning failure) to 2:

$$FF \in [0, 1, 1.5, 2] \quad 2$$

FF was calculated by evaluating the spacings between parallel filaments in the mask and identifying the smallest hatching distance where all filaments remained distinct without merging. This index assesses the printing resolution capability for parallel filament constructs.

Additionally, the Filament Diameter (FD) was computed as the average diameter along the filament (Fig. 2c). However, due to the high correlation with PI, subsequent analysis focused solely on the PI index.

2.5. Data analysis

An image analysis approach was employed to evaluate printability. For each iteration of the experiment, a final print image was captured using the in-situ HD Camera Tool and analyzed using MATLAB R2022a. All images were segmented to distinguish the print from the background, generating a mask corresponding to the printed layer's geometry. This mask facilitated the analysis of specific zones of the print, crucial for estimating printability parameters.

Data extracted from the images were analyzed using Minitab® 21.3.1. A linear model was applied to the PI dataset, with regressors computed through Ordinary Least Square regression (OLS). OLS relies on minimizing the square residuals [37] for model development.

In the case of FF analysis, a logistic regression was employed to model the discrete domain of the dataset. The logistic regression model, also known as a logit model, is a statistical tool for binary classification [39]. This approach utilizes a binomial cumulative distribution function to model the data and was computed directly in MATLAB R2022a. The software was also used for plotting all result graphs. In creating the models for this study, only significant terms were retained, ensuring the preservation of the hierarchical principle.

A comprehensive workflow framework is illustrated in Fig. 3.

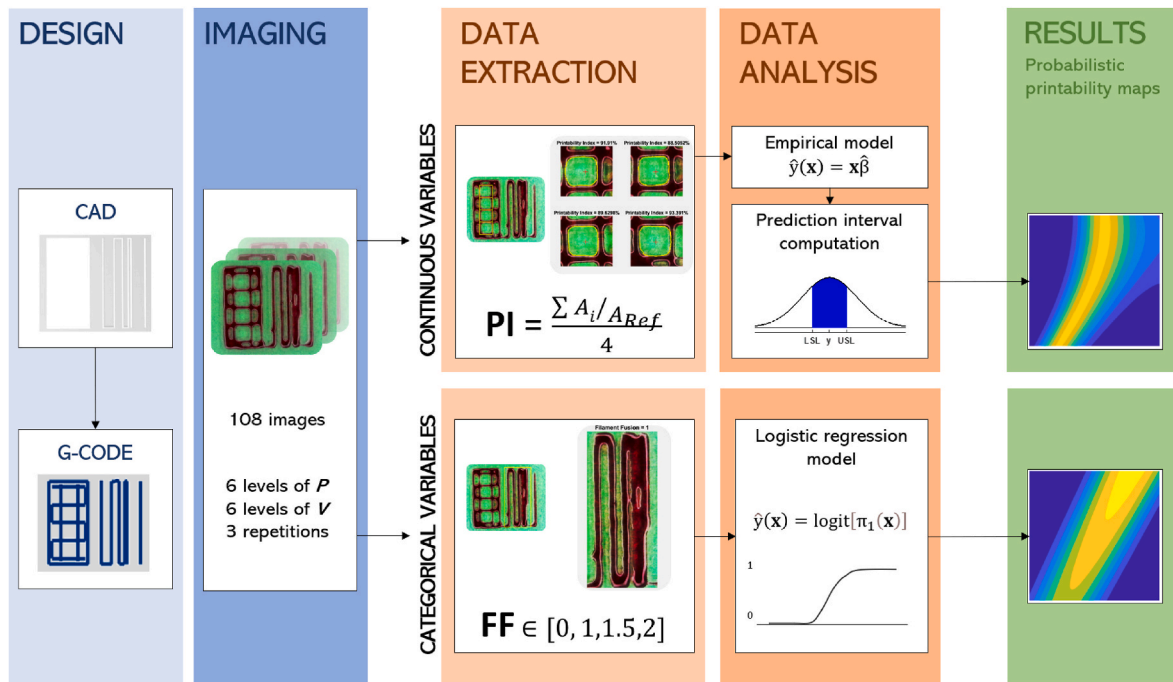


Fig. 3. Workflow of methods and results.

3. Results and discussions

Following the designated assumptions and methods, in-situ images of the printing samples were extracted to calculate the printability indexes, namely PI and FF (method workflow is depicted in Fig. 3). The measurements were organized in two structured datasets separately analyzed in the following sections.

3.1. Printability map for the PI quality feature

The experimental data overview is presented in Fig. 3. An empirical model was computed utilizing the OLS method, considering both Pressure and Speed as regressors and incorporating their interactions up to the second order. Three outliers with absolute standard residual errors larger than 3 were removed and the model was recalculated. The models are entirely quadratic in P and V. The Anderson-Darling test and the Ljung-Box Q-Test (LBQ) test on the Autocorrelation Function (ACF) were conducted on the residuals to validate the assumptions of normality and time independence, respectively [37]. Both tests failed to reject the null hypothesis (P -value > 0.05), confirming positive validation of all residual assumptions regarding normality and time independence. The results of the regression and residual checks are presented in Table S1 (Supplemental Materials).

Given the Gaussian data assumption, the prediction standard deviation of the model can be estimated as per Montgomery (2013):

$$\Delta(\mathbf{x}) = \sqrt{\text{MSE} \left(1 + \mathbf{x}^T (\mathbf{X}^T \mathbf{X})^{-1} \mathbf{x} \right)} \quad 3$$

where \mathbf{x} is the vector of regressors in the prediction location, and \mathbf{X} is the experimental data matrix. Once fixed the specification limits of the response, namely Lower Specification Limit (LSL) and Upper Specification Limit (USL), it was possible to estimate the prediction probability to observe the response $y(\mathbf{x})$ within the specification interval.

This probability can be calculated using the Student's T cumulative distribution function (F_{T,df_E}) as:

$$P(\mathbf{x}) = \text{Probability}\{LSL \leq y(\mathbf{x}) \leq USL\} \\ = F_{T,df_E} \left(\frac{USL - \hat{y}(\mathbf{x})}{\Delta(\mathbf{x})} \right) - F_{T,df_E} \left(\frac{LSL - \hat{y}(\mathbf{x})}{\Delta(\mathbf{x})} \right) \quad 4$$

As $\Delta(\mathbf{x})$ varies based on the prediction location, the width of the t-student distribution changes across the domain. Consequently, the probability is influenced not solely by the absolute Mean Squared Error (MSE), but also by the prediction location. As the location of the prediction varies, the width of the t-student distribution changes as well. Fig. 4 illustrates the response iso-lines of the empirical model and the probability calculation at three distinct locations within the domain, aiming to achieve a prediction within the previously defined acceptable range.

The theoretical optimal value is $PI = 1$, as defined in Equation (1), representing the scenario where $A_i = A$. An acceptable specification interval containing this value can be established. The selection of this interval is arbitrary and depends on the desired quality specifications. For this study, a non-symmetric interval encompassing the optimal value ($PI = 1$) was chosen, defined by $LSL = 0.60$ and $USL = 1.20$. This choice was based on the consideration that underextrusion ($PI > 1$) poses a greater risk than overextrusion ($PI < 1$), as it can lead to discontinuous flow, impacting the structural integrity of the constructs.

The probabilistic printability map can be computed in the entire experimental domain, as shown in Fig. 5.

3.2. Printability maps for FF via logistic regression

The FF analysis data are categorical and organized into classes. Printing failure was categorized into two distinct classes: underextrusion and overextrusion. Experimental tests characterised as successful prints

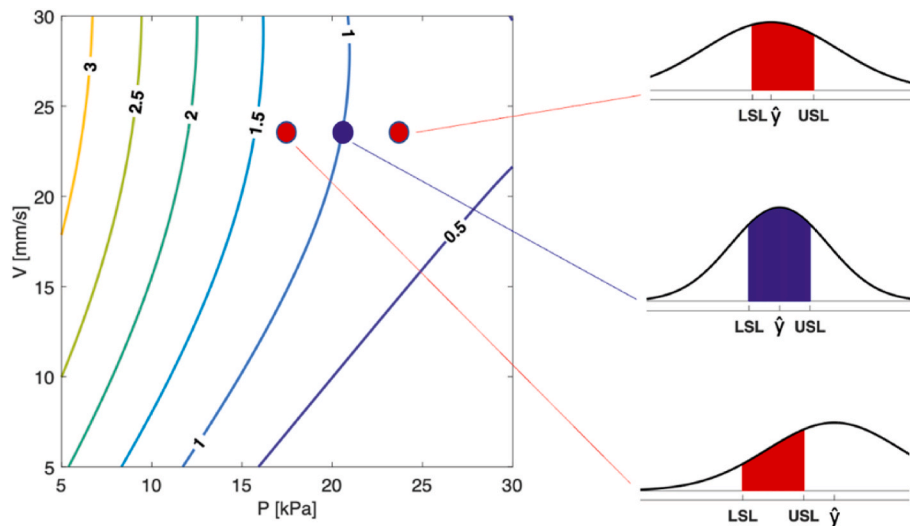


Fig. 4. PI empirical model with respect to the probabilities 3 single prediction locations around one of the optimal points with PI = 1.

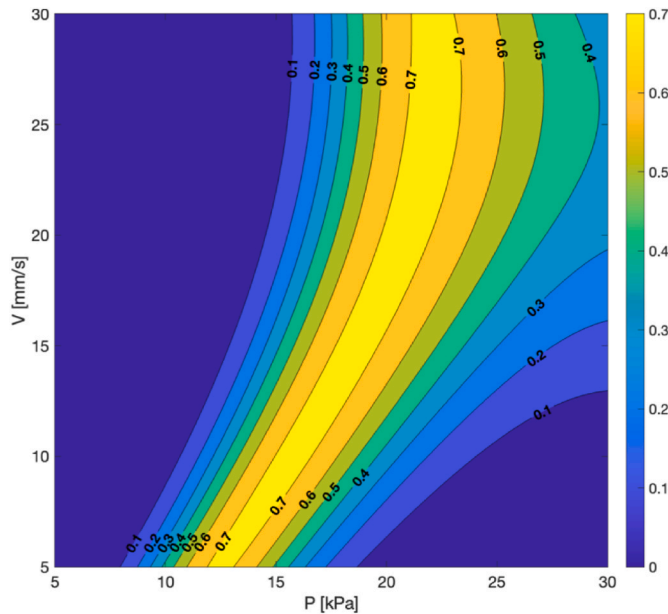


Fig. 5. Printability map of PI for LSL = 0.60 and USL = 1.20.

were classified into three classes, denoted as 1, 1.5, and 2, as defined previously. Due to the categorical nature of the data, two logistic models were constructed [39] to estimate the probability of encountering printing failure due to either underextrusion or overextrusion. These models utilized a binary column as the response variable, taking a value of 1 when the respective failure behavior was observed and null in the case of printing success. Both models were first order and exhibited satisfactory performance in explaining experimental data ($R_{adj}^2 = 71.9\%$ for the over-extrusion model, $R_{adj}^2 = 84.96\%$ for the under-extrusion model).

Despite their simplicity, these models distinctly delineate the different regions within the parameter domain: acceptable printing, failure due to overextrusion, and failure due to underextrusion. This map provides the operator with an overview of the acceptable process

window, its boundaries, and the width of the transition region (refer to Fig. 6).

Additional analysis was carried out to comprehensively characterize the process capabilities regarding printing resolution within the specified quality boundaries. Unlike the PI index, it was challenging to establish a specification interval (LSL and USL) where the printing outcome was universally acceptable in the case of FF. Instead, a success score was assigned to the discrete domain values of FF. This score, ranging from 0 to 1, represents the frequency of printing success. Consequently, the data were transformed according to Table 2.

Utilizing this data, the binomial distribution of the index was estimated based on the logistic regression fit. The logistic regression was performed as a Generalized Linear Model (GLM) [39] using the 'fitglm' function in MATLAB [40]. The model, a complete second-order model, considered the response variable f , representing the assigned printing score. The 'logit' link function was applied to fit the data using a binomial distribution.

The probability of having a successful printing modeled by a continuous function:

$$\hat{f}(\mathbf{x}) = \text{logit}[\pi_1(\mathbf{x})] = \ln\left(\frac{\pi_1(\mathbf{x})}{1 - \pi_1(\mathbf{x})}\right) = \mathbf{x}\hat{\beta} \quad 5$$

The $\pi_1(\mathbf{x})$ function expresses the probability of having a positive outcome according to the specification above defined. The probabilistic FF printability plotted in the parameters domain (Fig. 7) assumes the same meaning as the map explained in the previous Paragraph, but was obtained from a categorical index. The identified logistic model parameters are shown in Table S3. The interaction term $P \cdot V$ is kept in the model to preserve the complete hierarchical structure. The model had an $R_{adj}^2 = 61.79\%$.

The ink's performance was influenced by its physical properties, such as viscosity and gelification. This behavior implies that the optimal operating point might lie outside the considered domain of process parameters. However, as previously described for this specific application, increasing the scanning speed could result in machine instability. The probabilistic mapping approach can be employed with the ultimate goal of discovering an improved formulation. This involves attempts to either expand or relocate the optimal area within the feasible process boundaries by fine-tuning the bioink formulation.

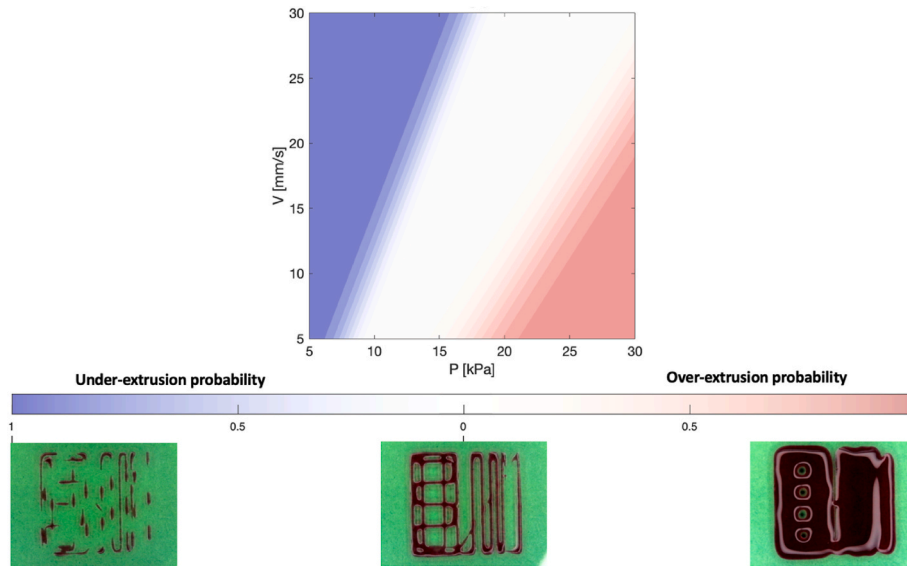


Fig. 6. Under and overs extrusion probabilistic maps in the parameters domain.

Table 2

FF values and relative assigned score.

FF value	Assigned score
0	0
2	0.33
1.5	0.67
1	1

The maximum score, denoted for $FF = 1$, was attributed to represent optimal process performance. Subsequent values within the successful printing range were assigned decreasing scores at equal intervals. A score of 0 was assigned for $FF = 0$, indicating failed experiments resulting from over or under extrusion without differentiation between the two.

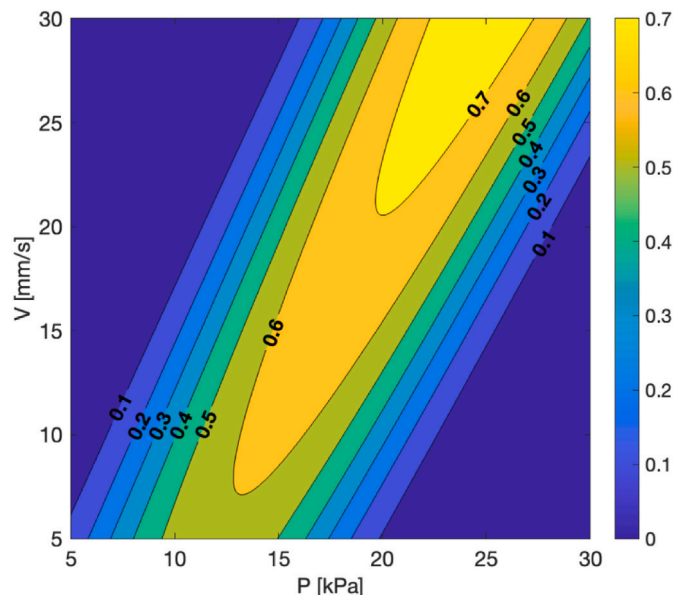


Fig. 7. Printability map of FF.

4. Discussion and sensitivity analysis

The in-situ printability maps illustrated in Figs. 5 and 7 depict the probability distribution of printability for the two analyzed quality indexes.

For PI, the region with the highest probability forms a band-like shape encompassing all speed ranges, indicating a broad optimal zone. In contrast, for FF, the optimal region is confined to the top-right corner of the domain. This limitation is due to the tendency of filaments to merge when extruded slowly, suggesting a need to expand the speed limit domain, although this expansion might impact process stability.

Given the strong dependence of the probability maps on the chosen specification limits, a sensitivity analysis was conducted to examine the effect of these limits on the maps. Three cases were considered: case 0, with the original specifications; case -1, with more relaxed specifications; and case +1, with tighter specifications. The procedure was applied to both models, involving different specifications as detailed in Table 3 and Table 4. The maximum probability output was observed for each map variation.

Regarding PI, the optimal range amplitude was varied while keeping the position of $PI = 1$ fixed within the interval. The values of LSL and USL were adjusted consistently with their distance from $PI = 1$, considering that overextrusion failure is preferred over underextrusion.

To visually represent the variation in the probability map, Fig. 8 illustrates zones where the probability exceeds 55 % for all model variations across both indexes.

Table 3

Sensitivity analysis for the probabilistic map of the PI. The base case (Case 0) is compared in terms of the maximum probability reached by the model with one characterised by a more relaxed specification (Case -1) and another with tighter specifications (Case +1). Values of the LSL and USL set are shown with also the range amplitude.

Case	-1	0	+1
Specifications	More relaxed	Base case	Tighter
Range amplitude	0.75	0.60	0.45
LSL	0.50	0.60	0.70
USL	1.50	1.20	1.15
Max probability	93.02 %	72.59 %	58.85 %

For FF, the minimum acceptance value represented by a unitary score was modified, scaling the remaining levels from 1 to 0 (representing printing failures) at evenly spaced intervals.

Table 4

Sensitivity analysis for the probabilistic map of the FF. The base case (Case 0) is compared in terms of the maximum probability reached by the model with one characterised by a more relaxed specification (Case -1) and another with tighter specifications (Case +1). In this case, specifications are expressed in terms of scoring values assignment.

Case		-1	0	+1
Specifications		More relaxed	Base case	Tighter
FF scoring table	Failure	0	0	0
	FF=2	0.5	0.33	0.25
	FF=1.5	1	0.67	0.50
	FF=1	1	1	0.75
Max probability		93.55 %	75.33 %	59.46 %

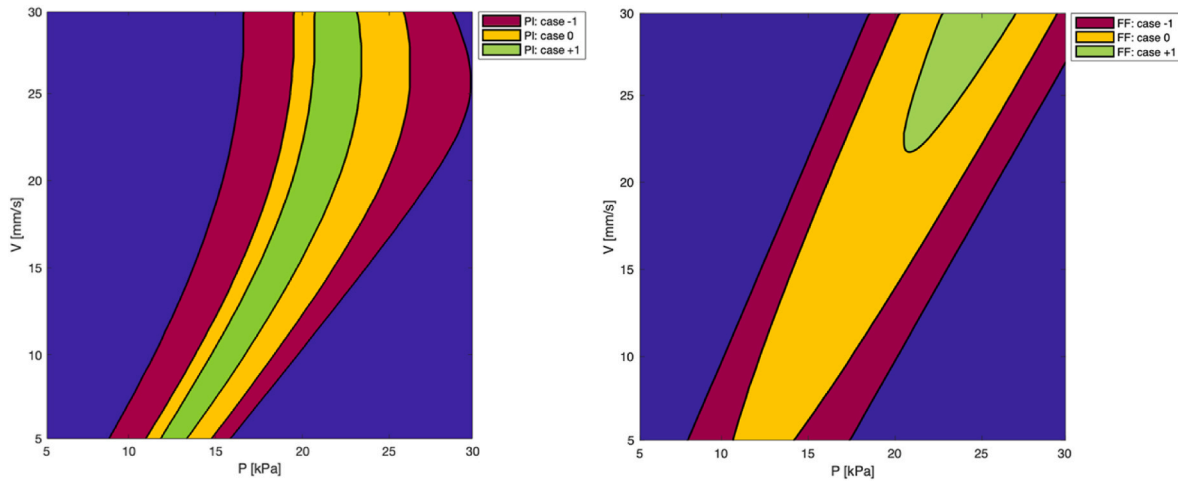


Fig. 8. Areas of the parameter domains characterised by a probability higher than 55 % for the three cases on the sensitivity analysis, grouped by index: PI (left) and FF (right).

The analysis revealed distinct behaviors of the two models. For PI, altering the specification range led to a scaled probability map where the maximum probability value increased or decreased while maintaining the same shape (Fig. 8).

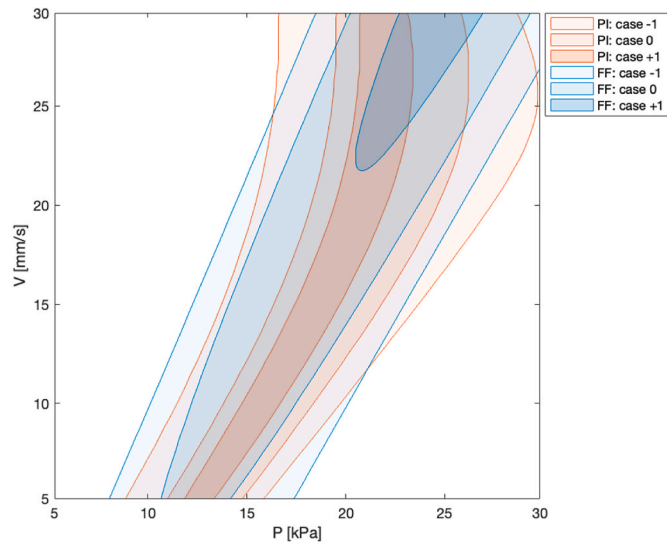


Fig. 9. Areas of the parameter domains characterised by a probability higher than 55 % for the three cases on the sensitivity analysis for the two indexes superimposed.

Regarding FF, tighter specifications pushed the optimal area toward higher values of pressure and speed, extending beyond the domain. In bioprinting, as in other manufacturing processes, different quality indexes can exhibit dissimilar behaviors. In such cases, a multi-index analysis proves valuable, providing operators with a comprehensive understanding of the process. The divergent behavior is evident in Fig. 9, where iso-probability areas for both indexes are overlaid in the same graph. Depending on the specified criteria, overlapping acceptable areas for both indexes can be identified. This method proves powerful in pinpointing optimal operating points and feasible specification prescriptions associated with one or more quality indexes.

5. Robust printability maps for bioprinting with living cells

After determining the optimal region using the IPM, cells can be incorporated into the process for a comprehensive bioprinting assessment. Given the higher cost and delicacy associated with bioprinting involving cells, our suggested approach involves introducing cells after identifying the optimal region using the robust printability map. Introducing cells might in principle alter the rheological properties of the bioink, even if this effect is known to be relevant only when significant levels of concentration are considered [36]. In our case, a 10 % solution of cell suspension (following the cell mixing protocol by Cellink) was added in place of the 10 % Amaranth solution, ensuring minimal impact on the overall rheology due to the low cell density used.

In our study, we specifically evaluated the viability of murine myoblasts C2C12 cells to understand if specific settings within the optimal region adversely affect the cells. C2C12 myoblasts were chosen to assess the viability of skeletal muscle cells in edible bioinks, relevant for cultured meat production. As mentioned earlier, IPMs are valuable for

Table 5

Pressures and Speed of the three conditions analyzed for the cell viability.

Sample N°	P [kPa]	V [mm/s]
1	10	1
2	20	20
3	30	25

process optimization, particularly for large-scale bioprinting such as in cultured meat production. We investigated the effect of shear stress induced by the optimal pressure in the nozzle via bioprinting at three representative points within the IPM domain. As indicated in Figs. 8 and 9, the optimal printing region for the studied case depended on the specifications and could be identified within the pressure range of 10 kPa–30 kPa.

To ensure equal expected viability throughout the IPM's optimal printing area, we examined three points within the process domain (Table 5). A 7.5 mm long filament structure was bioprinted in a M24 well for each condition, with four replicas for each. The constructs were monitored for up to three days after bioprinting, and viability was assessed using Live/Dead staining (Table S4) according to the protocol defined in Section 2.

The bars in Fig. 10 display viability data for each day. Error bars represent one standard deviation above and below the mean. According to ANOVA within each day, no significant differences were observed ($\alpha = 0.05$). (b) An in-situ image of a printed construct (P = 30 kPa and V = 25 mm/s). Scale bar 1 mm. (c) A Live/Dead image after processing, illustrating the viability of a sample printed with the same parameters above, evaluated on day 1 after printing. Scale bar 100 μ m.

No significant differences among process parameters were observed within each day (P -value >0.05, Table S5 in the Supplemental material). Therefore, within the domain considered for the IPM, the process did not negatively impact cell viability. This allows experimenters to select the bioprinting operating point solely based on process-related factors (e.g., productivity, deposition time, energy consumption), disregarding the potential impact of printing parameters on cell viability within the specified domain, as it proves to be non-harmful.

6. Conclusions

The introduction of probability maps presents a groundbreaking approach to exploring the printability of bioinks, marking a departure from current methods, which largely rely on qualitative approaches or empirical models. While empirical models are valuable for interpreting processes and finding optimal parameters, they have limitations. They offer a single-point prediction for optimal parameters, disregarding the inherent variability in the printing process and measurement systems. As a result, they do not provide a feasible range of the final printing outcome, accounting for the probability of achieving the desired quality.

Probability maps, as facilitated by IPMs, address these limitations. They identify high-quality operational regions within the parameter domain, visually representing the domain and acceptance region boundaries. These maps facilitate the identification of optimal printing parameters, enabling diverse approaches to guide the search process. For instance, operators can optimize the search within a larger domain to find zones more resilient to parameter variations or identify zones with a higher probability of successful outcomes. Furthermore, the probability maps approach allows for multi-index optimization. Combining multiple IPMs constructed on different quality indexes helps identify portions of the domain that satisfy multiple quality conditions simultaneously.

The probabilistic maps method, based on the logistic model, offers a valid alternative to regression models, especially when quantifying the nature of the response is challenging. This is particularly relevant in the field of extrusion bioprinting, where quality specification limits are less stringent and don't require precise measurement systems compared to other additive manufacturing processes. Visual inspection becomes more convenient for classifying printing outcomes. This enables operators to quickly investigate probability maps based on the target quality of the specific application, especially in the initial stages of new material or product development.

Additionally, as the printability maps approach relies on in-line and in-situ imaging, it is well-suited for adaptive experimental sampling. This represents a significant advancement toward rapid and in-line printability assessment. Standardizing quality assessment methods and establishing robust process mapping and optimization techniques are pivotal for transitioning bioprinting technology from the laboratory to industrial applications. Therefore, probabilistic IPMs can also be applied to optimize process scalability. Operators can set print acceptance as a

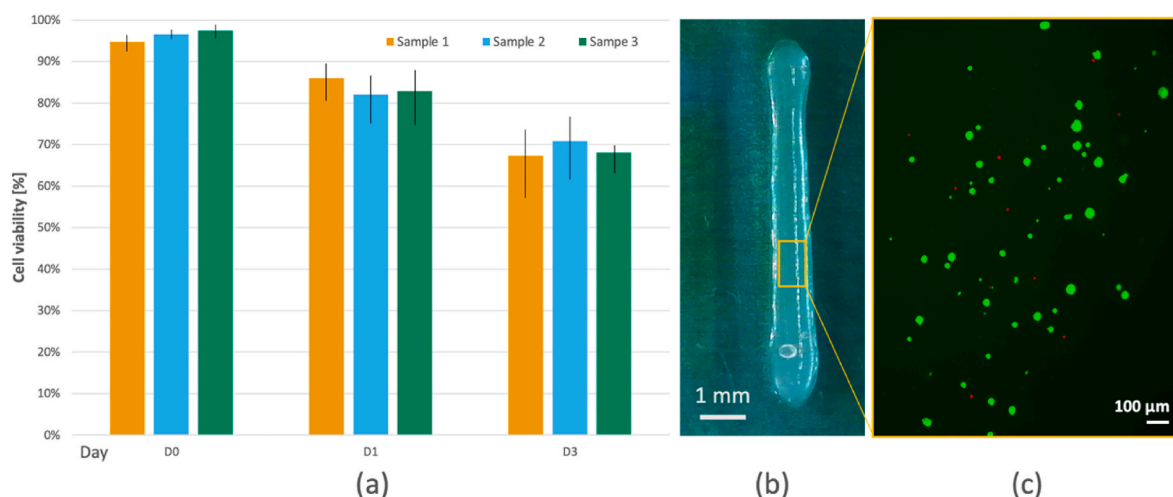


Fig. 10. (a) Viability of the Murine Myoblasts cells in AlGel bioink deposited with extrusion bioprinting at the three tested conditions of P and V. The histogram shows viability data for each day. Error bars represent a sample standard deviation above and below the mean. According to ANOVA within each day, no significant difference is observed ($\alpha = 0.05$). (b) In-situ image of a printed construct (P = 30 kPa and V = 25 mm/s). Scale bar 1 mm. (c) An example of a Live/Dead image after the processing (P = 30 kPa, V = 25 mm/s, day 1 after printing). Scale bar 100 μ m.

constraint and, within the highest probability of acceptance area, define various optimization functions. These functions could focus on maximizing printing speed (reducing printing times) or minimizing energy consumption (correlating the compressor and motion motors to their relative consumption).

Ultimately, IPMs, relying on statistical modeling, pave the way for the development of digital twins and closed-loop controllers for the bioprinting process, representing a significant step forward in the evolution of bioprinting technologies.

Funding

This research was partially funded by the European Union under the “HORIZON-CL4-2021-DIGITAL- EMERGING-01 project BioProS - Bio-intelligent Production Sensor to Measure Viral Activity” (grant agreement no. 101070120), 2022–2026.”

CRediT authorship contribution statement

Giovanni Zanderigo: Conceptualization, Data curation, Formal analysis, Investigation, Methodology, Software, Validation, Visualization, Roles, Writing – original draft, Writing – review & editing. **Filippo Bracco:** Conceptualization, Data curation, Formal analysis, Investigation, Methodology, Software, Validation, Visualization, Roles, Writing – original draft, Writing – review & editing. **Quirico Semeraro:** Conceptualization, Data curation, Formal analysis, Methodology, Project administration, Supervision, Validation, Writing – review & editing. **Bianca Maria Colosimo:** Conceptualization, Formal analysis, Funding acquisition, Methodology, Project administration, Resources, Supervision, Validation, Writing – review & editing.

Declaration of competing interest

The authors declare that they have no known competing financial interests or personal relationships that could have appeared to influence the work reported in this paper.

Data availability

Data will be made available on request.

Acknowledgments

The Authors acknowledge Davide Moscatelli and his support in the 3D Cell Lab.

Appendix A. Supplementary data

Supplementary data to this article can be found online at <https://doi.org/10.1016/j.bprint.2023.e00320>.

References

- [1] S. Santoni, S.G. Gugliandolo, M. Sponchioni, D. Moscatelli, B.M. Colosimo, 3D bioprinting: current status and trends—a guide to the literature and industrial practice, *Bio-Design and Manufacturing* 5 (1) (Jan. 01, 2022) 14–42, <https://doi.org/10.1007/s42242-021-00165-0>. Springer.
- [2] W.L. Ng, C.K. Chua, Y.F. Shen, Print me an organ! Why we are not there yet, *Prog. Polym. Sci.* 97 (Oct. 01, 2019), <https://doi.org/10.1016/j.progpolymsci.2019.101145>. Elsevier Ltd.
- [3] Z. Fu, S. Naghieh, C. Xu, C. Wang, W. Sun, X. Chen, Printability in extrusion bioprinting, *Biofabrication* 13 (3) (Jul. 01, 2021), <https://doi.org/10.1088/1758-5090/abe7ab>. IOP Publishing Ltd.
- [4] K. Nair, et al., Characterization of cell viability during bioprinting processes, *Biotechnol. J.* 4 (8) (2009) 1168–1177, <https://doi.org/10.1002/biot.200900004>.
- [5] T. Gao, et al., Optimization of gelatin-alginate composite bioink printability using rheological parameters: a systematic approach, *Biofabrication* 10 (3) (Jun. 2018), <https://doi.org/10.1088/1758-5090/aacdc7>.
- [6] J.H.Y. Chung, et al., Bio-ink properties and printability for extrusion printing living cells, *Biomater. Sci.* 1 (7) (2013) 763–773, <https://doi.org/10.1039/c3bm00012e>.
- [7] Y. Zhao, Y. Li, S. Mao, W. Sun, R. Yao, The influence of printing parameters on cell survival rate and printability in microextrusion-based 3D cell printing technology, *Biofabrication* 7 (4) (Nov. 2015), <https://doi.org/10.1088/1758-5090/7/4/045002>.
- [8] J. Lee, S.J. Oh, S.H. An, W.D. Kim, S.H. Kim, S.H. Kim, Machine learning-based design strategy for 3D printable bioink: elastic modulus and yield stress determine printability, *Biofabrication* 12 (3) (Jul. 2020), <https://doi.org/10.1088/1758-5090/ab8707>.
- [9] N. Diamantides, et al., Correlating rheological properties and printability of collagen bioinks: the effects of riboflavin photocrosslinking and pH, *Biofabrication* 9 (3) (Jul. 2017), <https://doi.org/10.1088/1758-5090/aa780f>.
- [10] S. Freeman, S. Calabro, R. Williams, S. Jin, K. Ye, Bioink formulation and machine learning-empowered bioprinting optimization, *Front. Bioeng. Biotechnol.* 10 (Jun. 13, 2022), <https://doi.org/10.3389/fbioe.2022.913579>. Frontiers Media S.A.
- [11] A. Pössl, D. Hartzke, T.M. Schmidts, F.E. Runkel, P. Schlupp, A targeted rheological bioink development guideline and its systematic correlation with printing behavior, *Biofabrication* 13 (3) (Jul. 2021), <https://doi.org/10.1088/1758-5090/abde1e>.
- [12] L. Ouyang, R. Yao, Y. Zhao, W. Sun, Effect of bioink properties on printability and cell viability for 3D bioplotting of embryonic stem cells, *Biofabrication* 8 (3) (Sep. 2016), <https://doi.org/10.1088/1758-5090/8/3/035020>.
- [13] N. Paxton, W. Smolan, T. Böck, F. Melchels, J. Groll, T. Jungst, Proposal to assess printability of bioinks for extrusion-based bioprinting and evaluation of rheological properties governing bioprintability, *Biofabrication* 9 (4) (Nov. 2017), <https://doi.org/10.1088/1758-5090/aa8dd8>.
- [14] G. Gillispie, et al., Assessment methodologies for extrusion-based bioink printability, *Biofabrication* 12 (2) (2020), <https://doi.org/10.1088/1758-5090/ab6f0d>. Institute of Physics Publishing.
- [15] A. Habib, V. Sathish, S. Mallik, B. Khoda, 3D printability of alginate-carboxymethyl cellulose hydrogel, *Materials* 11 (3) (Mar. 2018), <https://doi.org/10.3390/ma11030454>.
- [16] K.K. Moncal, V. Ozbolat, P. Datta, D.N. Heo, I.T. Ozbolat, Thermally-controlled extrusion-based bioprinting of collagen, *J. Mater. Sci. Mater. Med.* 30 (5) (May 2019), <https://doi.org/10.1007/s10856-019-6258-2>.
- [17] S.W. Sawyer, et al., 3D bioprinting optimization of human mesenchymal stromal cell laden gelatin-alginate-collagen bioink, *Biomed. Mater.* 18 (1) (Jan. 2023), <https://doi.org/10.1088/1748-605X/aca3e7>.
- [18] Y. He, F. Yang, H. Zhao, Q. Gao, B. Xia, J. Fu, Research on the printability of hydrogels in 3D bioprinting, *Sci. Rep.* 6 (Jul. 2016), <https://doi.org/10.1038/srep29977>.
- [19] C. Nelson, S. Tuladhar, L. Launen, M.D.A. Habib, 3D bio-printability of hybrid pre-crosslinked hydrogels, *Int. J. Mol. Sci.* 22 (24) (Dec. 2021), <https://doi.org/10.3390/ijms222413481>.
- [20] M. Hibbert, J.M. Viljoen, L.H. du Plessis, Print parameter optimisation for a Pluronic F-127 and alginate hybrid hydrogel, *Bioprinting* 30 (Apr. 2023), <https://doi.org/10.1016/j.bprint.2022.e00257>.
- [21] A. Ribeiro, et al., Assessing bioink shape fidelity to aid material development in 3D bioprinting, *Biofabrication* 10 (1) (Jan. 2018), <https://doi.org/10.1088/1758-5090/aa90e2>.
- [22] R. Suntornnond, E.Y.S. Tan, J. An, C.K. Chua, A mathematical model on the resolution of extrusion bioprinting for the development of new bioinks, *Materials* 9 (9) (Sep. 2016), <https://doi.org/10.3390/ma9090756>.
- [23] M. Temirel, S.R. Dabbagh, S. Tasoglu, Shape fidelity evaluation of alginate-based hydrogels through extrusion-based bioprinting, *J. Funct. Biomater.* 13 (4) (Dec. 2022), <https://doi.org/10.3390/jfb13040225>.
- [24] S. Coşkun, S.O. Akbulut, B. Sarıkaya, S. Çakmak, M. Gümüşderelioglu, Formulation of chitosan and chitosan-nanoHAP bioinks and investigation of printability with optimized bioprinting parameters, *Int. J. Biol. Macromol.* 222 (Dec. 2022) 1453–1464, <https://doi.org/10.1016/j.ijbiomac.2022.09.078>.
- [25] A.A. Armstrong, A. Pfeil, A.G. Alleyne, A.J. Wagoner Johnson, Process monitoring and control strategies in extrusion-based bioprinting to fabricate spatially graded structures, *Bioprinting* 21 (Mar. 2021), <https://doi.org/10.1016/j.bprint.2020.e00126>.
- [26] T. Guo, et al., 3D printing PLGA: a quantitative examination of the effects of polymer composition and printing parameters on print resolution, *Biofabrication* 9 (2) (Apr. 2017), <https://doi.org/10.1088/1758-5090/aa6370>.
- [27] J.E. Trachtenberg, et al., Extrusion-based 3D printing of poly(propylene fumarate) in a full-factorial design, *ACS Biomater. Sci. Eng.* 2 (10) (Oct. 2016) 1771–1780, <https://doi.org/10.1021/acsbiomaterials.6b00026>.
- [28] A.A. Armstrong, A.G. Alleyne, A.J. Wagoner Johnson, 1D and 2D error assessment and correction for extrusion-based bioprinting using process sensing and control strategies, *Biofabrication* 12 (4) (2020), 045023. <https://doi.org/10.1088/1758-5090/aba8ee>.
- [29] A.A. Armstrong, J. Norato, A.G. Alleyne, A.J. Wagoner Johnson, Direct process feedback in extrusion-based 3D bioprinting, *Biofabrication* 12 (1) (2020), 015017. <https://doi.org/10.1088/1758-5090/ab4d97>.
- [30] J. Shin, Y. Lee, Z. Li, J. Hu, S.S. Park, K. Kim, Optimized 3D bioprinting technology based on machine learning: a review of recent trends and advances, *Micromachines* 13 (3) (Mar. 01, 2022), <https://doi.org/10.3390/mi13030363>. MDPI.
- [31] K. Rubner, et al., Coupling machine learning with 3D bioprinting to fast track optimisation of extrusion printing, *Appl. Mater. Today* 22 (Mar. 2021), <https://doi.org/10.1016/j.apmt.2020.100914>.
- [32] A.F. Bonatti, G. Vozzi, C.K. Chua, C. De Maria, A deep learning quality control loop of the extrusion-based bioprinting process, *Int. J. Bioprint* 8 (4) (2022) 307–320, <https://doi.org/10.18063/ijb.v8i4.620>.

- [33] B.M. Colosimo, E. del Castillo, L.A. Jones-Farmer, K. Paynabar, K. Artificial intelligence and statistics for quality technology: an introduction to the special issue, *J. Qual. Technol.* 53 (5) (2021) 443–453.
- [34] P. Parenti, D. Puccio, B.M. Colosimo, Q. Semeraro, A new solution for assessing the printability of 17-4 PH gyroids produced via extrusion-based metal AM, *J. Manuf. Process.* 74 (Feb. 2022) 557–572, <https://doi.org/10.1016/j.jmapro.2021.12.043>.
- [35] V. Bodiou, P. Moutsatsou, M.J. Post, Microcarriers for upscaling cultured meat production, *Front. Nutr.* 7 (Feb. 20, 2020), <https://doi.org/10.3389/fnut.2020.00010>. Frontiers Media S.A.
- [36] N. Diamantides, C. Dugopolski, E. Blahut, S. Kennedy, L.J. Bonassar, High density cell seeding affects the rheology and printability of collagen bioinks, *Biofabrication* 11 (4) (Aug. 2019), <https://doi.org/10.1088/1758-5090/ab3524>.
- [37] D.C. Montgomery, *Design and Analysis of Experiments*. Eighth Edition, 2013.
- [38] Dirk-Jan Kroon, *Region Growing*, 2023.
- [39] A. Agresti, *An Introduction to Categorical Data Analysis Second Edition*, 2007.
- [40] A.J. Dobson, *An Introduction to Generalized Linear Models*, 2002.